Interactions of 22-MeV He^3 Particles with $Fe^{56,58}$ and Ni^{58} †

EDWARD R. FLYNN AND LOUIS ROSEN
Los Alamos Scientific Laboratory, University of California, Los Alamos, New Mexico
(Received 18 August 1966)

A systematic study is made of the interaction of 22-MeV He^3 ions with $Fe^{56,58}$ and Ni^{58}. The central purpose of this study is to compare the interactions induced by this strongly absorbed, spin-$\frac{1}{2}$ particle to various theoretical interpretations which have been successfully applied to the more commonly used nuclear probes: neutrons, protons, and alpha particles. The present investigation encompasses elastic and inelastic scattering as well as the spectral distribution of emitted neutrons of energy greater than 0.5 MeV. The elastic-scattering data are analyzed both in terms of an optical model and a strong-absorption model. The inelastic-scattering data and the high-energy neutron data are compared to the predictions of distorted-wave Born-approximation calculations. Finally, the low-energy neutron data are analyzed within the framework of the compound-nucleus model, and nuclear temperatures are extracted.

I. INTRODUCTION

THE use of He^3 ions in the study of nuclear interactions has increased considerably during the past several years as a result of the greater availability of pure He^3 and the application of recirculating systems in accelerators to conserve its use.[1] The utility of this projectile as a nuclear probe is well established, especially in the field of nuclear spectroscopy, where its extensive use has yielded a large amount of new information about the structure and properties of nuclear levels.

Among the more significant applications of the He^3 particle as a nuclear probe are the (He^3,d) reaction studies of Blair *et al.*,[2–4] aimed at the examination of single-particle proton states. A variety of experiments utilizing the (He^3,n) reaction to produce proton-rich nuclei also has been reported,[5–7] indicating further the value of He^3 beams. Elastic-scattering experiments involving these particles have been undertaken for a variety of target nuclei and at a number of energies.[3,8–10]

Recently, several inelastic-scattering experiments involving He^3 ions have been reported.[11–13]

A number of theoretical investigations of He^3-induced reactions appear in the literature. Henley and Yu[14] have given an extensive analysis of the (He^3,n) reaction, assuming that it proceeds via a direct interaction. Application of the optical model to the elastic-scattering problem has been made by Hodgson[15] and others,[8] and good agreement with experimental data is obtained.[16] At present, theoretical analyses have not extended to inelastic data, but the methods which have been developed by Bassel *et al.*[17] should be applicable to He^3 particles also.

In all of the work thus far reported, the motivations have not included the detailed investigation of the possibly unique characteristics of the He^3 interaction, and it is this goal which is foremost in the present studies. For this reason a set of experiments involving several of the possible modes of interaction available to an He^3 ion impinging on a nucleus was carried out. The modes to be described are elastic scattering, direct interaction via inelastic scattering and double stripping, and compound-nucleus formation via the (He^3,n) reaction. The immediate purpose of these investigations was to examine the ways in which the He^3 ion differs from the more common projectiles, such as nucleons and α particles. A secondary objective was to explore the possibility of additional applications of He^3 beams in nuclear structure studies.

II. EXPERIMENTAL APPARATUS

The experimental data required for a comprehensive investigation of He^3-induced interactions necessitate a variety of experimental techniques. This section will describe the scattering chamber for charged particles, the liquid-hydrogen bubble chamber, the nuclear emulsion technique, and, finally, the multiradiator neutron telescope.

† Work performed under the auspices of the U. S. Atomic Energy Commission.

[1] H. E. Wegner and W. S. Hall, Rev. Sci. Instr. **29**, 1100 (1958).
[2] A. G. Blair, Argonne National Laboratory Report No. ANL 6878, 1964, p. 115 (unpublished).
[3] D. D. Armstrong, Ph.D. thesis, University of New Mexico, 1965 (unpublished).
[4] A. G. Blair and E. R. Flynn, Bull. Am. Phys. Soc. **10**, 495 (1965).
[5] G. U. Din, J. L. Weil, and G. C. Phillips, Argonne National Laboratory Report No. ANL 6848, 1964, p. 199 (unpublished).
[6] J. H. Manley, Phys. Rev. **130**, 1475 (1963).
[7] H. C. Bryant, J. G. Beery, E. R. Flynn, and W. T. Leland, Nucl. Phys. **53**, 97 (1964).
[8] D. D. Armstrong, R. H. Bassel, and A. G. Blair (to be published).
[9] H. M. Sen Gupta, J. Rotblat, E. A. King, and J. B. A. England, Nucl. Phys. **50**, 549 (1964).
[10] P. E. Hodgson, in *Proceedings of the Rutherford Jubilee International Conference, Manchester, 1961* (Academic Press Inc., New York, 1961), p. 407.
[11] E. R. Flynn, Bull. Am. Phys. Soc. **10**, 540 (1965).
[12] E. F. Gibson, J. J. Kraushaar, and M. E. Rickey, Bull. Am. Phys. Soc. **10**, 539 (1965).
[13] R. H. Siemssen, T. H. Braid, D. Dehnhard, and B. Zeidman, Bull. Am. Phys. Soc. **10**, 540 (1965).
[14] E. M. Henley and D. U. L. Yu, Phys. Rev. **133**, B1445 (1964).
[15] P. E. Hodgson, Nucl. Phys. **21**, 28 (1960); **23**, 499 (1961).
[16] G. Igo, Phys. Rev. **115**, 1665 (1959).
[17] R. H. Bassel, G. R. Satchler, R. M. Drisko, and E. Rost, Phys. Rev. **128**, 2693 (1962).

A. Scattering Chamber for Charged Particles

The elastic- and inelastic-scattering experiments were performed in a 20-in. scattering chamber using silicon solid-state detectors. The detectors were located on an arm which could be moved about the target with extreme precision by means of a radar antenna control system. This was done remotely so that no interruption of cyclotron operation was necessary. It was also possible to change targets remotely by raising or lowering the target shaft—as many as five targets being available on this shaft.

Three detectors were used during the experiments. One of these, a 500-μ surface-barrier unit, was located on a separate arm from the main detector and served as a monitor; the other two were mounted on the radar arm mentioned above and were used for the angular distribution measurements. The latter two detectors consisted of a 100-μ transmission unit followed by a 500-μ surface-barrier unit. These detectors were mounted against each other so that they made up a $\Delta E \times E$ mass identification system. The monitor detector was used to indicate beam location shifts or target breakage during the data taking. The separation of He^3 particles from α particles in this detector system was sufficient to permit accurate cross-section measurements.

A beam of 22-MeV He^3 ions from the cyclotron was energy-analyzed by a 90° bending magnet located just before the scattering chamber. The beam passed through $\frac{1}{16}$-in. slits at the entrance and exit focal positions of the magnet with the emergent beam, $\sim\frac{1}{16}$ in. in its largest dimension, focused on the target. The energy resolution of the beam entering the scattering chamber was ~40 keV full width at half-maximum (FWHM), and the maximum intensity was 0.6 μA. The over-all resolution of the detector system was 70 keV, including detector resolution and electronic noise. This resolution does not include target-thickness effects.

The targets used were metal foils prepared by electrochemical deposition in the case of the two Fe targets and by vacuum evaporation for the Ni target. Target nonuniformity limited the absolute determination of the target density exposed to the beam to $\pm 15\%$, and this is the dominant uncertainty in the absolute cross section. Somewhat better precision was obtained by normalizing to the theoretical Rutherford scattering at forward angles.

The minimum angle of measurement for the elastic scattering data was 9°. Data were taken in 3° intervals out to 150°.

The minimum angle for inelastic scattering was determined by how well the nonelastic peaks could be extracted from the large elastic component caused by multiple small-angle scattering in the slit edges, with degradation of the primary beam energy. This angle varied somewhat depending upon the magnitude of the inelastic-scattering cross section. For example, it was 18° for the 2^+ state of the Fe isotopes and 24° for the Ni^{58} target. The 3^- states could not be clearly resolved below 27° for all three targets.

The data peaks were fit, by a computer program, to a skewed Gaussian curve so that the appropriate areas under each peak could be extracted for cross-section determination. Past experience with cyclotron data has indicated that the skewed Gaussian shape provides a good representation of the data peaks and permits not only the area determination, but also an accurate location of the peak position for energy determination.

B. Bubble Chamber

A liquid-hydrogen bubble chamber was one of the three instruments employed to measure the neutron spectra produced by the bombardment of the three isotopes by the He^3 beam. With this instrument, neutrons from 5 to 35 MeV could be detected and their energies measured. The bubble chamber application to neutron spectroscopy has previously been reported and a number of experimental results published.[7,18–20]

The present work was designed to measure the angular distributions of the neutrons emitted from the targets and required modifications to the experimental arrangement previously reported. The bubble chamber was mounted upon a frame which was anchored to a shaft located directly below the target, thus forming an axis of rotation for the entire bubble chamber assembly. The chamber was free to rotate over a total angular interval of -20 to $+75$°. In the experiments to be described, as in previous work, the bubble chamber was located outside of the usual cyclotron experimental room in order to provide additional shielding from neutrons.

The Fe and Ni targets for the neutron experiments were in the form of rolled metallic foils and consisted of enriched separated isotopes of these metals. Directly behind each target was located a 0.020-in.-thick gold foil in which the 22-MeV He^3 beam was stopped. The entire target assembly was then insulated from the beam tube and connected to an electrometer so that it would function as a Faraday cup.

A method of pulsing the cyclotron beam was required commensurate with the pulsed bubble chamber operation. The conditions for sensitivity as well as the manner of pulsing both bubble chamber and cyclotron have been described in Ref. 18. The repetition rate of the chamber was set at 20 pulses per minute and a sensitive time of 4 msec during each pulse. The cylcotron beam was adjusted to 3-msec duration and was initiated 0.5 msec after the chamber had become sensitive. In this manner, some margin of safety with regard to instability in timing of the two pulses could be obtained. The timing pulses were continuously monitored

[18] E. R. Flynn and P. J. Bendt, Rev. Sci. Instr. **33**, 223 (1962).
[19] E. R. Flynn and P. J. Bendt, Phys. Rev. **128**, 1268 (1962).
[20] E. R. Flynn, M. S. thesis, University of New Mexico, 1961 (unpublished).

by an oscilloscope, which displayed simultaneously the bubble chamber pressure pulse and the output of a scintillation detector. This detector, located immediately adjacent to the target, responded to the γ rays generated by the beam pulse impinging upon the target assembly.

The experimental data were taken at 10° intervals over a total angular region of 0° to 50°. At each angle, the three targets and an empty target assembly were exposed to the cyclotron beam, and approximately 1600 pictures were taken for each of the targets.

It was necessary to measure about 34 000 pairs of photographs in order to obtain adequate cross-section information; each stereo pair contained an average of seven tracks. To perform the measurements, a film viewer of special construction was used. It projected the two stereo views simultaneously on a screen, where the measurements were performed in semi-automated fashion and the data recorded on IBM cards. The measuring rate was about 100 tracks per hour. This instrument and the method of measurement are described in Refs. 7 and 18.

C. Nuclear Emulsions

To investigate the low-energy spectrum of neutrons emitted from the three targets, it was necessary to employ a second method of measurement in addition to the bubble chamber. A nuclear emulsion technique[21] has been used extensively in the low-energy region and allows the measurement of neutron energies down to 0.5 MeV. Since emulsion efficiency remains relatively high even above 5 MeV, it was possible to overlap the bubble chamber data and compare the absolute cross sections derived by the two methods.

The photographic plates were placed around the targets from 10° to 150° in 20° intervals. The emulsions were supported by thin wires so that no appreciable neutron scattering could occur from the supports. The distance of the front edge of the emulsions from the target was 10 cm. To reduce background from extraneous sources, the emulsion detectors were located in the same experimental area as the bubble chamber which, as mentioned previously, was well shielded by the additional walls of the cyclotron experimental vault. In addition, instead of stopping the beam directly in back of the target, as in the case of the bubble chamber experiments, the beam was allowed to continue an additional 6 ft to be stopped in a gold foil. With this arrangement, the solid angle subtended by the emulsion at the beam stopper was small enough that low-energy neutrons coming back from the gold did not cause a serious background problem. Both 200- and 400-μ plates were exposed simultaneously to ensure sufficient detection efficiency.

The processing and measurement of the photographic plates followed the procedures outlined in Ref. 21.

[21] L. Rosen, Nucleonics **11**, 32 (1953), Part I.

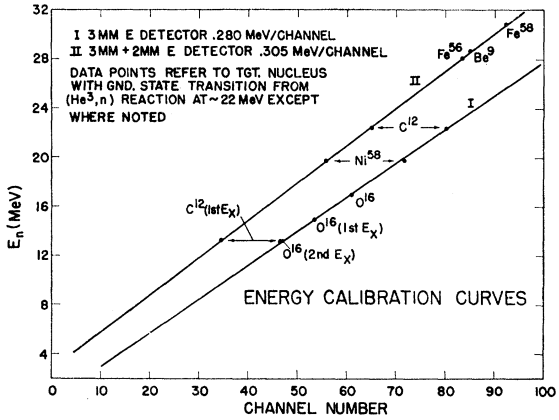

FIG. 1. Energy calibration curve for neutron counter.

Following subtraction of background and the elimination of tracks outside of the accepted angular limits, about 400 good events remained for each plate examined. The procedure for converting the flux of proton recoils measured in the emulsion into a flux of incident neutrons was as described in Ref. 21.

D. Solid-State Neutron Detector

To complete the study of the neutron spectra emitted from the Ni^{58} and $Fe^{56,58}$ targets, the angular distributions of the neutrons corresponding to the ground state of the residual nucleus were measured. Although the bubble chamber is a high-efficiency neutron detector over a wide energy range, it was not adequate to allow a precise determination of the high-energy portions of the neutron spectra without an inordinate number of pictures. A better approach, in this case, was to use a detector in which the detection efficiency could be maximized at the energy to be measured, while still retaining adequate resolution to separate the ground-state neutrons from those associated with excited states. The absence of the requirement of a wide-energy range, such as the bubble chamber possesses, suggested the use of a neutron telescope. The energies to be measured were too high for other methods, such as time-of-flight. On the other hand, neutron telescopes have been used frequently in the 15- to 30-MeV energy region, although mainly for observing monoenergetic neutron groups.[22]

The neutron telescope developed for this problem differs from the conventional style of these detectors, in that use is made of solid-state transmission detectors to achieve higher efficiency and lower background counting rates. The manner in which this is done has been fully described in a previous publication.[23] In this instrument, the single radiator of the ordinary counter telescope has been replaced by a sandwich of

[22] S. J. Bame, Jr., E. Haddad, J. E. Perry, Jr., and R. K. Smith, Rev. Sci. Instr. **28**, 997 (1957).

[23] E. R. Flynn and H. C. Bryant, Rev. Sci. Instr. **37**, 215 (1966).

radiators and solid-state transmission detectors. The detector in which the recoil proton is stopped, the E detector, is a lithium-drifted silicon detector of 3- or 5-mm depletion depth. The multiradiator assembly is located 25 cm from the target, and with 300-mm^2 area circular radiators an acceptance angle of $\pm 2°$ was achieved—the same as with the bubble chamber.

The radiator sandwich consists of five polyethylene foils interspaced with five 200-μ silicon transmission detectors. The area of each of these is slightly larger than the 300 mm^2 mentioned above, but a 0.050 in. tantalum aperture located directly behind the sandwich defines the useful area of the system. The radiators are mounted on wheels to permit various thicknesses of polyethylene to be rotated into place depending on the energy of the neutron to be observed. There is also a blank position in each of the wheels so that data can be taken with no radiators in place to obtain the contribution of recoil protons due to all background sources, such as the silicon in the transmission detectors.

Uncertainties in energy are introduced by: (1) the first-encountered radiator thickness since the proton recoil can occur anywhere within this radiator and (2) the variance in the recoil proton angle caused by the finite solid angle of the E detector. This signal is then amplified and fed into a 100-channel section of a multichannel analyzer. To minimize background effects from neutron reactions in the E detector and from wall reactions, the analyzer accepts only events which arrive simultaneously with a gating pulse from a coincidence circuit. This coincidence pulse is generated whenever signals from the last transmission detector and the E detector arrive together, assuring that the proton detected has indeed come from the radiator package.

To establish an energy calibration so that energy assignments could be made to observed peaks, it was necessary to obtain energy spectra of several elements with known levels. The reactions used for this purpose were the following: $C^{12}(He^3,n)O^{14}$, $O^{16}(He^3,n)Ne^{18}$, and $Be^9(He^3,n)C^{11}$. The spectra taken at zero degrees are

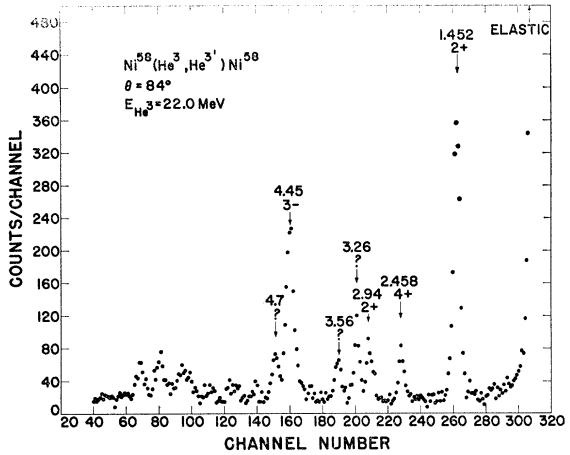

FIG. 2. Typical inelastic spectrum.

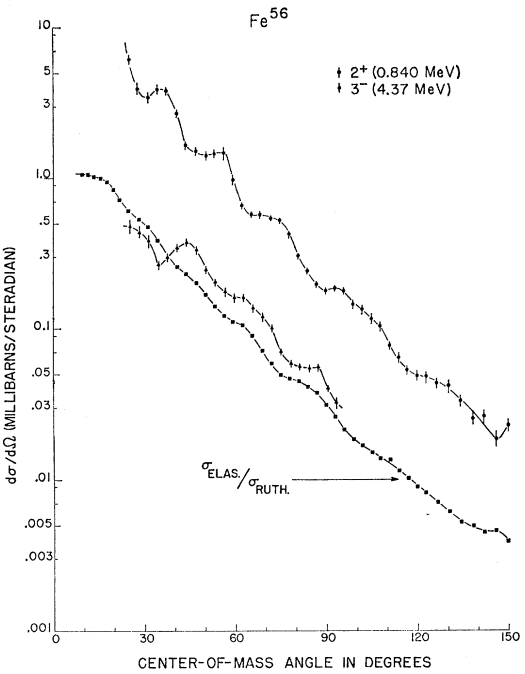

FIG. 3. Elastic and inelastic data for Fe^{56}.

shown in the Appendix. In Fig. 1, the resulting graph of the energy calibration is shown: curve I was used for the Ni^{58} target, and curve II was used for the higher energy neutrons obtained from the $Fe^{56,58}$ targets.

The efficiency of the counter telescope has been calculated using the approximate expression given by Bame *et al.*[22] for each detector, and the method is described in Ref. 23.

It has been assumed that a larger uncertainty exists in the cross-section determination than in the energy regions which encompass the structure in the efficiency curve. This is due mainly to the uncertainties in the level of cutoff pulse, which will just trigger the coincidence circuit, as well as to the actual thicknesses of the radiators and transmission detectors involved in the proton-range calculations. However, the main purpose of the counter-telescope has been the measurement of high-energy neutrons involving the smooth part of the curve. Extension of the use of the counter into lower energies has been investigated, and the C^{12} and O^{16} targets have given good agreement with earlier results obtained with the liquid-hydrogen bubble chamber,[7] indicating that the above-mentioned uncertainties are not insurmountable. Also, evidence will be shown in later discussion for excellent overlap of neutron spectra obtained from the Fe^{58} target by means of the bubble chamber and with the neutron-counter telescope.

III. EXPERIMENTAL RESULTS

Figure 2 is a typical example of a 400-channel spectrum on which are indicated a number of the known

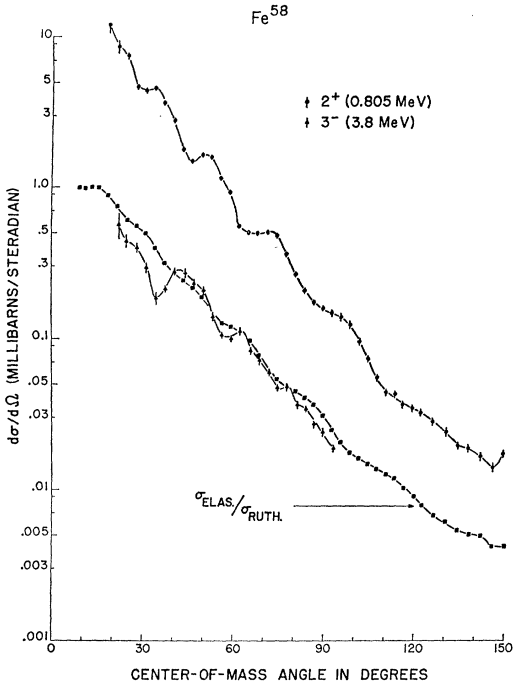

FIG. 4. Elastic and inelastic data for Fe^{58}.

energy levels of the target nucleus. The results of the elastic- and inelastic-scattering experiments are shown in Figs. 3–5. In these figures, the elastic data have been divided by the corresponding Rutherford cross section before plotting in order to emphasize the structure due to nuclear effects. The elastic and inelastic 2^+ cross sections for Fe^{58} have been corrected for the 21% Fe^{56} content of the target.

Although the oscillations in the differential cross sections are considerably depressed by Coulomb effects, a definite phase relation between the three cross sections for each target is apparent. In each case, the 2^+ is seen to be out of phase with the corresponding elastic cross section and the 3^- state, the latter two being in phase with each other. This effect is to be expected and has been predicted by Blair[24] on the basis of a simple diffraction model of elastic and inelastic scattering.

An example of the spectra of low-energy neutrons as observed with nuclear emulsions is shown in Fig. 6 for the Fe^{56} target and for all of the angles which were analyzed. The typical magnitudes of the errors for various neutron energies are indicated in the uppermost curve of the figure, and similar errors apply to all the curves below. Actually, photographic plates were exposed every 20°, but only those represented in the figures were analyzed, because the main region of interest in obtaining compound-nucleus information lies in the backward hemisphere. To the extent that the neutrons are emitted from a compound nucleus, the differential cross sections will be isotropic at these angles. The 30° plates were included for the purpose of cross-checking measured cross sections between the photographic emulsion method and the bubble chamber method, which extends down to 5 MeV and encompasses measurements at 30°. All of the data shown are corrected for background.

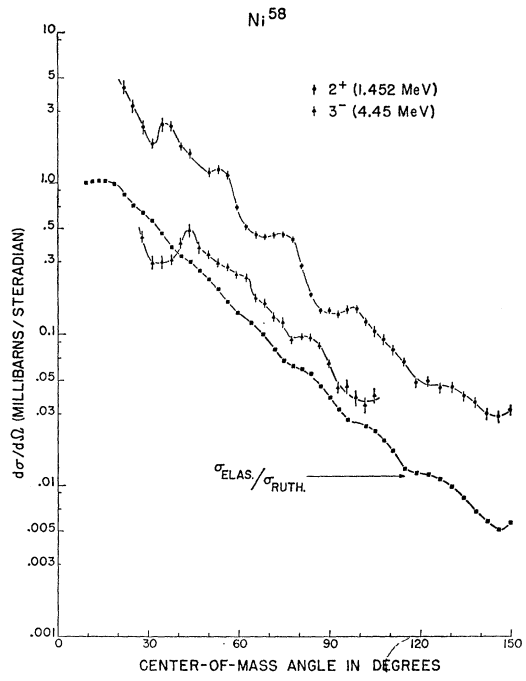

FIG. 5. Elastic and inelastic data for Ni^{58}.

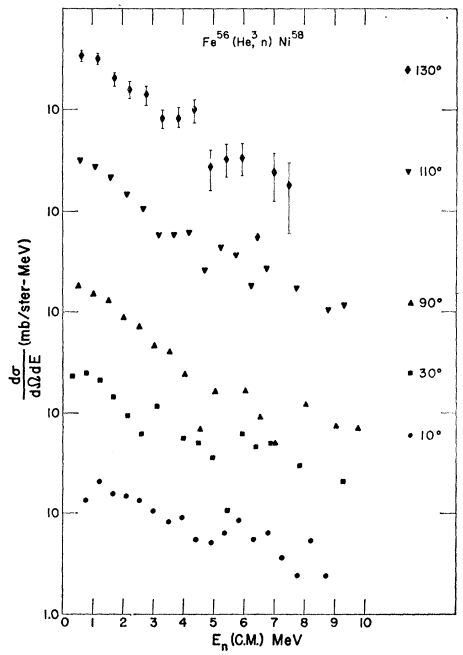

FIG. 6. Low-energy neutron spectra for Fe^{56}.

[24] J. S. Blair, Phys. Rev. **115**, 928 (1959).

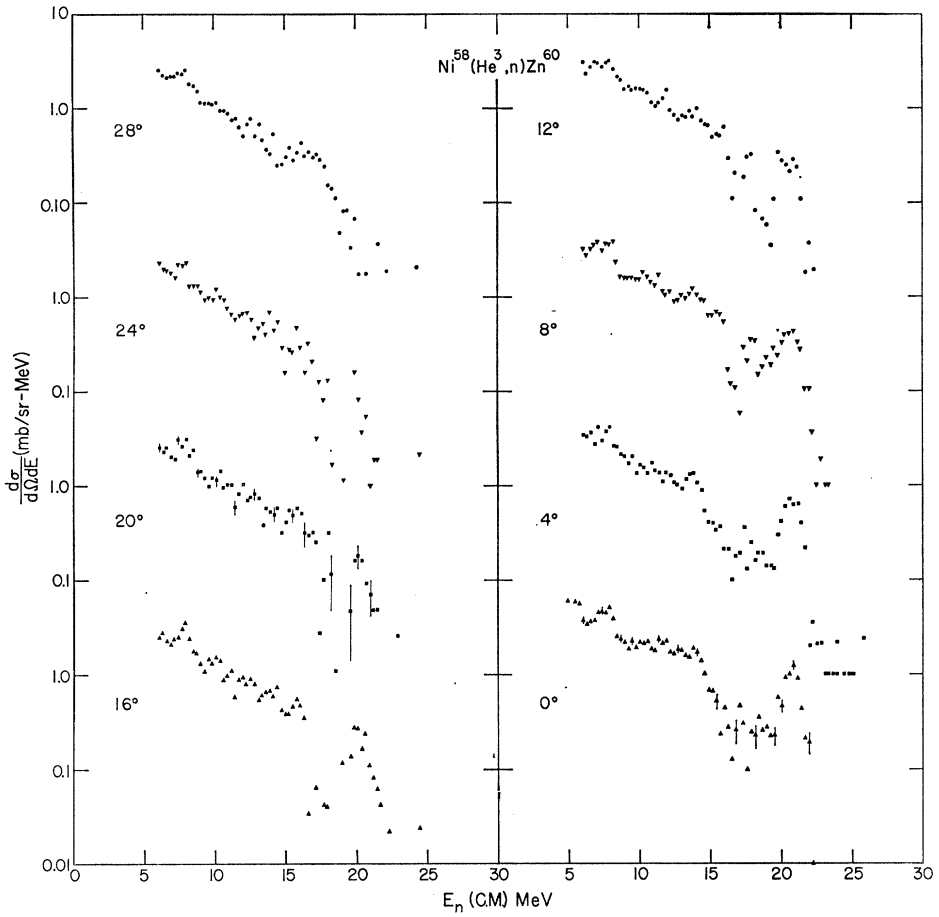

FIG. 7. High-energy neutron spectra for Ni^{58}.

Figure 7 displays the data obtained from the multiradiator neutron telescope for the Ni^{58} target. Since the main use of this device was to investigate the forward-peaked direct-interaction neutrons, only the region close to 0° was examined. The interval between data points was dictated by the amplifier gain and the use of 100 channels of the pulse-height analyzer. For Ni^{58} this step is 0.280 MeV. For the Fe isotopes it is 0.305 MeV, because the higher neutron energies required a lower amplifier gain. The low-energy cutoff occurring in the region of 7 to 8 MeV is for the reasons discussed in Ref. 23.

Figure 7 clearly illustrates the predominance of direct interactions at forward angles. The ground-state yield rises substantially above the extrapolated slope of the data at higher excitation energies.

Since the bubble chamber data overlapped the emulsion data at low energies and the neutron-counter telescope data at high energies, it was possible to perform an internal self-consistency check on the accuracy of the absolute-cross-section measurements. The 30° angle was selected for this purpose, and Fig. 8 indicates the result for Fe^{58}. The agreement between the bubble chamber data and the counter data (the counter was actually located at 28°) is excellent, and although the statistics in this energy region for the emulsion data preclude an accurate comparison, these data also seem to be in qualitative agreement.

IV. THEORETICAL ANALYSIS OF THE DATA

In this section theoretical descriptions of the data will be developed corresponding to the three types of data to be treated: elastic-scattering, direct interactions, and compound-nucleus reactions. The elastic-scattering analyses will be described first in terms of an optical model and then in terms of a strong-interaction diffraction model. Direct-interaction analyses will be made by means of the distorted-wave Born-approximation (DWBA) method and both inelastic scattering and (He^3,n) ground-state transitions will be treated in this way. Finally, reactions proceeding through a compound nucleus will be examined in terms of an evaporation model.

A. Elastic-Scattering Analysis

1. Optical Model

The most general method of describing elastic-scattering data is through the use of the complex potential, or optical model. Although this approach is phenom-

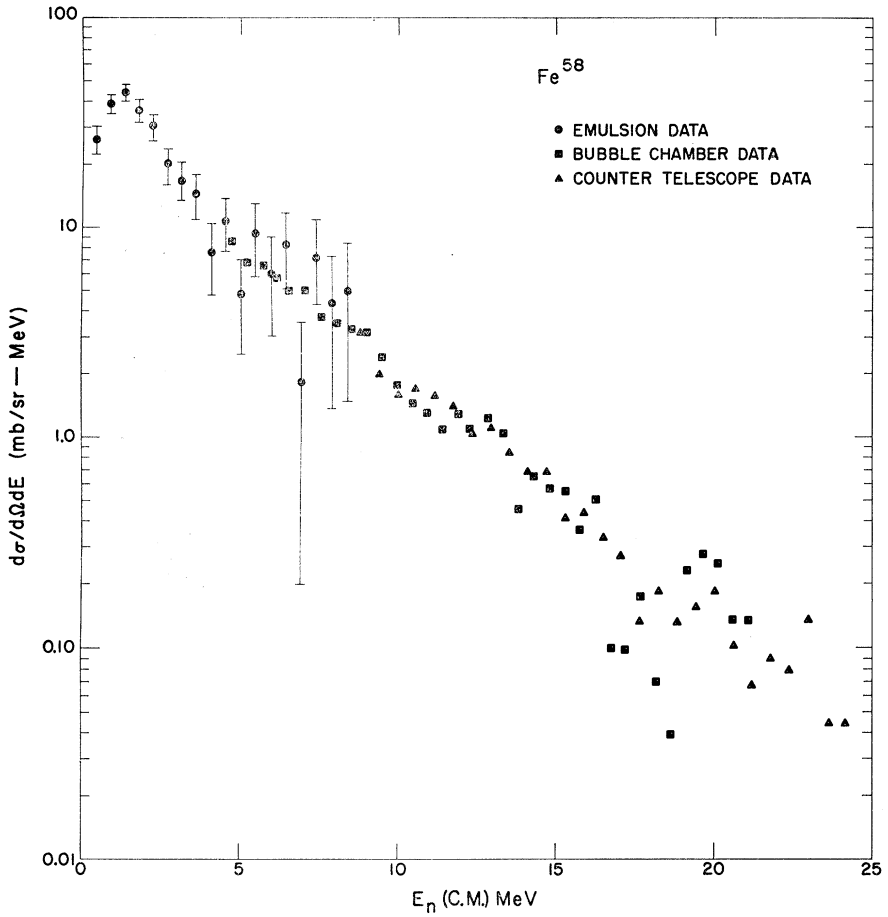

FIG. 8. Neutron spectra at 30° from Fe^{58} over energy range from 0.5 to 30 MeV.

enological in nature, it makes possible the correlation of large amounts of data as a function of energy and nuclear species. The model parameters refer to the average properties of the target nucleus and are useful in the prediction of cross sections and polarizations and in DWBA calculations. This last use applies whether the particle is in the entrance or exit channel of the DWBA calculation. Because of these many applications, numerous systematic surveys of elastic scattering of protons,[25,26] neutrons,[27] deuterons,[28] and α particles[16] have been carried out. A major goal of these endeavors has been to establish energy and mass dependence of the parameters which characterize the optical-model potential. Unfortunately, there are inadequate data on the elastic scattering of He^3 ions to allow the determination of systematic trends, although a few results have been published.[10]

The potential form and range of parameters adopted here were based on those suggested by Bassel.[8] These have the feature that their real potential is approximately three times as strong as the real potential for nucleons. Since the He^3 particle contains three nucleons and is only weakly bound, this choice seems appropriate, and the elastic scattering of a number of elements has been well described with it. The form of the potential is

$$V=-[Uf(x)+iWf(x')],$$

where

$$f(x)=\left[1+\exp\left(\frac{r-R_r}{a_r}\right)\right]^{-1};$$
$$f(x')=\left[1+\exp\left(\frac{r-R_i}{a_i}\right)\right]^{-1}. \quad (1)$$

The values of the parameters were determined by using a χ^2 minimum fitting routine available in an optical-model code by Perey.[26] Table I lists the parameter set which is thought best and which is used in all subsequent calculations. The fits to the data are shown in Fig. 9. It should be pointed out that the parameters are not unique, since several other parameter sets give results which cannot be distinguished from the present ones.

[25] L. Rosen, J. G. Beery, A. S. Goldhaber, and E. H. Auerbach, Ann. Phys. (N. Y.) 34, 96 (1965).
[26] F. G. Perey, Phys. Rev. 131, 745 (1963).
[27] L. Rosen, in Proceedings of the International Conference on the Study of Nuclear Structure with Neutrons, Antwerp, Belgium, 1965 (unpublished).
[28] C. M. Perey and F. G. Perey, Phys. Rev. 132, 755 (1963).

Two points concerning the form of the potential are worth noting. The first of these is that no spin-orbit term is necessary to describe the elastic-scattering data even as far back in angle as 150°. The second point is that a derivative form for W, much used in the literature for protons and neutrons, is not needed. However, the strong absorption present here might very well explain this feature. Since the absorption takes place at a large radius, and within a narrow range of this radius, there is no need to introduce a faster rising potential.

2. *Strong-Absorption Model*

An alternative means of analyzing the elastic scattering of He^3 particles is by means of a strong-absorption model.[29] The basis for this approach lies in the assumption that all partial waves below a certain value will be completely absorbed. This implies that only a limited region of angular-momentum space contributes to the reaction. The advantages of this method are that the absorptive mechanism need not be known and the introduction of potentials is not required. In the discussion to follow, the strong-absorption model will be developed and the results compared with the data. The strong-absorption parameters which best describe the data will then be compared with similar parameters obtained from the optical-model calculations, and discrepancies will be discussed.

The method used here is that of Frahn and Venter[30–34] and is a phenomenological approach assuming an arbitrary shape for the phase shifts describing the scattering process. The differential cross section for elastic scattering may be written as

$$\sigma(\theta)=|A(\theta)|^2+|B(\theta)|^2, \tag{2}$$

where A and B are scattering amplitudes and are obtained from the general scattering amplitude

$$f(\theta)=\frac{i}{2k}\sum_{l=0}^{\infty}[(l+1)(1-\eta_l^+)+l(1-\eta_l^-)]\exp(2i\sigma_l)$$
$$-\frac{i}{2k}(\mathbf{n}\cdot\boldsymbol{\sigma})\sum_{l=0}^{\infty}(\eta_l^+-\eta_l^-)\exp(2i\sigma_l)$$
$$\times\frac{d}{d\theta}P_l(\cos\theta)+f_c(\theta). \tag{3}$$

In (3), η_l is the scattering function to be defined below, $f_c(\theta)$ is the Coulomb scattering amplitude, σ_l is the Coulomb phase shift, and k is the wave number (momentum/$\hbar$). A is then defined to be the first summation plus $f_c(\theta)$, and B is the summation involving the derivative of the Legendre polynomials.

The scattering functions appearing in Eq. (3) are then assumed to have the following form:

$$\mathrm{Re}\eta_l^{\pm}=g^{\pm}(l+\tfrac{1}{2}), \tag{4}$$

$$\mathrm{Im}\eta_l^{\pm}=\mu^{\pm}dg^{\pm}(l+\tfrac{1}{2})/dt, \tag{5}$$

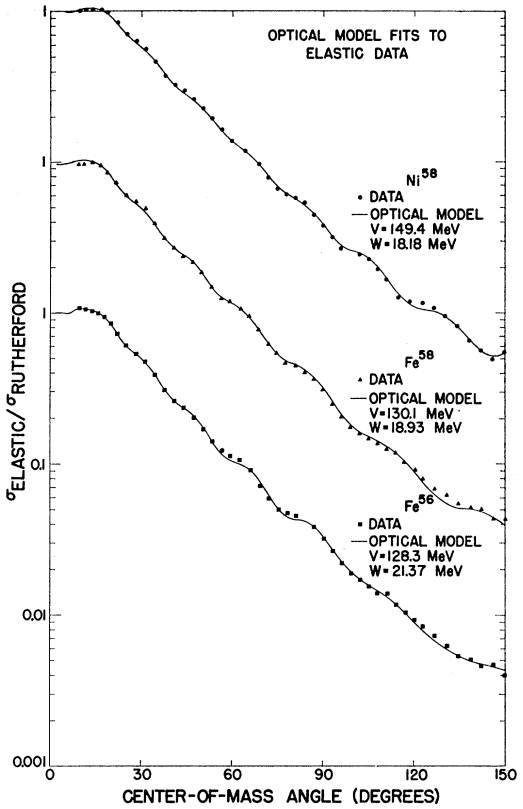

FIG. 9. Optical-model fits to elastic scattering.

TABLE I. Optical-model and strong-absorption parameters which are used here to describe the elastic-scattering data.

	Fe^{56}	Fe^{58}	Ni^{58}
		Optical model	
V	128.3 MeV	130.1 MeV	149.4 MeV
W	21.37 MeV	18.78 MeV	18.18 MeV
r_r (R_r)	1.08 (4.13)F	1.08 (4.18)F	1.08 (4.18)F
r_i (R_i)	1.56 (5.97)F	1.56 (6.04)F	1.63 (6.13)F
a_r	0.816F	0.770 MeV	0.767F
a_i	0.734F	0.787 MeV	0.765F
r_c (R_c)	1.25 (4.78)F	1.25 (4.84)F	1.25 (4.84)F
σ_R	1.34b	1.38b	1.37b
		Strong absorption	
R	8.08F	8.02F	8.12F
d	0.52F	0.51F	0.49F
μ^+	1.12	1.12	1.07
μ^-	−0.72	−0.72	−0.82
σ_R	1.34b	1.31b	1.27b

[29] J. S. Blair, Phys. Rev. **95**, 1218 (1954).
[30] W. E. Frahn and R. H. Venter, Ann. Phys. (N. Y.) **24**, 243 (1963).
[31] R. H. Venter, Ann. Phys. (N. Y.) **25**, 405 (1963).
[32] W. E. Frahn and R. H. Venter, Ann. Phys. (N. Y.) **27**, 135 (1964).
[33] R. H. Venter and W. E. Frahn, Ann. Phys. (N. Y.) **27**, 385 (1964).
[34] R. H. Venter and W. E. Frahn, Ann. Phys. (N. Y.) **27**, 401 (1964).

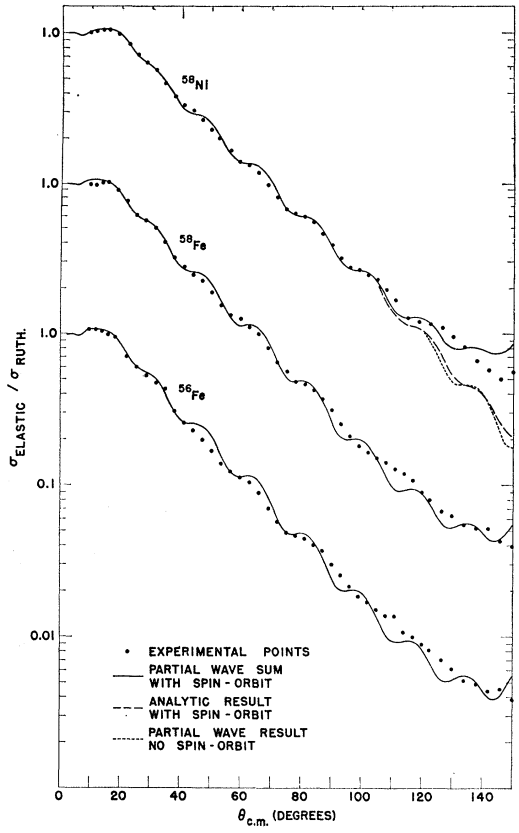

FIG. 10. Strong-absorption fits to elastic scattering.

and the quantities $g^{\pm}$ are considered as continuous functions of the angular momentum. They may be written

$$g^{\pm}=\left\{1+\exp\left[\frac{(L^{\pm}+\frac{1}{2})-(l+\frac{1}{2})}{\Delta_{\pm}}\right]\right\}^{-1}, \tag{6}$$

which is the familiar Woods-Saxon shape. Frahn and Venter have obtained an analytic expression for the cross section by replacing the summation in Eq. (3) with an integration. This procedure is described in Refs. 30–34. In Ref. 32 it is noted that a reasonable representation of the experimental data may be obtained by allowing $g^{+}=g^{-}$, which leaves four parameters: μ^{+}, μ^{-}, L, and Δ. The quantity L may be related to the interaction radius R by considering the classical description of Coulomb scattering of point particles. The angular momentum L corresponds to the case where the particles of momentum k are passing the nucleus at its absorption radius R, i.e., they are just "grazing" the edge.

Coulomb scattering theory then gives

$$R=\frac{1}{k}\{n+[(L+\tfrac{1}{2})^2+n^2]^{1/2}\}, \tag{7}$$

where n is the Coulomb parameter, $n=\mu^{z}1^{z}2e^2/\hbar^2k$.

In a similar way, Δ is related to a diffuseness parameter associated with the nuclear surface. Since this term represents an incremental change in l, it may be obtained from Eq. (7) by differentiation, noting that $\Delta=\delta l$ and $d=\delta R$; then

$$d=(\Delta/k)(1-2n/kR)^{1/2}/(1-n/kR). \tag{8}$$

A more accurate evaluation of the validity of the assumptions in Eqs. (4) and (5), by comparison of calculations based on them with experimental data, is possible if Eq. (3) is retained, instead of using the approximate analytic expression, and the summation over partial waves is done by means of a computer. This has been done and a χ^2 search routine employed to obtain the best fit to the data. These results are shown in Fig. 10, and the parameters obtained from this procedure are summarized in Table I. In addition, the Ni^{58} data are compared to the Frahn-Venter analytic result for these same parameters. Also illustrated for Ni^{58} is the result of a search in which $\mu^{+}=\mu^{-}$, which implies the absence of a spin-orbit term. There appears to be a definite discrepancy between the results given by Eq. (3) and the corresponding results given by the analytic formalism at large angles (beyond 110° in this case). This discrepancy is even more pronounced in the predicted polarization at these angles, inferring that the summation should be employed in this region.

B. Distorted-Wave Theory of Direct Interactions

The distorted-wave Born-approximation (DWBA) has had considerable success in accurately describing direct-interaction processes such as stripping and inelastic scattering. Since the theory is well described in the literature,[14,17,35] only an outline will be presented here with emphasis on the particular interaction modes which pertain to the experimental evidence contained in the present work.

The cross section describing a reaction taking place between an initial state i and final state f may be written

$$\frac{d\sigma}{d\Omega}=\left(\frac{\mu}{2\pi\hbar^2}\right)^2\frac{k_f}{k_i}\sum|T_{fi}|^2, \tag{9}$$

where the summation symbol represents an average of the transition amplitudes T_{fi}, μ is the reduced mass of the colliding pair of nuclei, and $\hbar k_f=P_f$ and $\hbar k_i=P_i$ are the final and incident momenta involved. The transition amplitude is then given in the Born approximation by

$$T_{fi}=\langle X_f^{(-)}(\mathbf{k}_f,\mathbf{r})\varphi_f|V|\varphi_i\chi_i^{(+)}(\mathbf{k}_i,\mathbf{r})\rangle$$

$$=\int d\mathbf{r}\,\chi_f^{(-)*}(\mathbf{k}_f,\mathbf{r})\langle\varphi_f|V|\varphi_i\rangle\chi_i^{(+)}(\mathbf{k}_i,\mathbf{r}). \tag{10}$$

[35] W. Tobocman, *Theory of Direct Nuclear Reactions* (Oxford University Press, New York, 1961).

The $\chi(\mathbf{k},\mathbf{r})$ are solutions of the same Schrödinger equation as was used to fit the elastic scattering, namely,

$$\left\{\nabla^2+k^2-\left(\frac{2\mu}{\hbar^2}\right)[V(r)-V_{\text{Coul}}(r)]\right\}\chi(\mathbf{k},r)=0, \quad (11)$$

with the various quantities the same as previously defined.

The quantity within the brackets in Eq. (10) is called the effective interaction and is the matrix element of the interaction taken between the internal states of the interacting nuclei. Following the development of Ref. 17, Eq. (9) may be written as

$$\frac{d\sigma}{d\Omega}=\frac{2J_f+1}{2J_I+1}\sum_l |A_l|^2\sigma_l(\theta), \quad (12)$$

where the A_l is related to the strength of the interaction or the spectroscopic amplitude and $\sigma_l(\theta)$ is calculated by DWBA computer codes for various types of form factors.[36] For the results described here, two types of form factors will be considered, the inelastic and the double stripping. With these belong appropriate values of A_l's which determine the strength of the interaction.

1. *Inelastic Scattering*

In the mass region of nuclides which have been considered in this investigation, the low-lying states of even-even nuclei are well described by a collective model assuming shape vibrations about a spherical core. This phenomenon has been described by Bohr and Mottelson.[37]

The shape of an arbitrary configuration may be described classically in the following way:

$$R=R_0[1+\sum_{l=0}^{\infty}\sum_{m=-l}^{l}\alpha_{lm}Y_l^m(\theta,\varphi)]. \quad (13)$$

The α_{lm} in Eq. (13) may then be considered as quantum-mechanical boson operators which create and annihilate phonons. Each phonon α_{lm}, according to Eq. (13), is equivalent to an oscillation of angular momentum l with z component m and parity $(-1)^l$.

The usual method of obtaining the collective form factor is to expand the elastic potential in a Taylor series about R_0, and then for the single-phonon case it is only necessary to keep the first derivative term and substitution of Eq. (13) gives, for a particular l and m,

$$V_{lm}^{(1)}=R_0\frac{dV}{dr}\alpha_{lm}Y_l^m(\theta,\varphi). \quad (14)$$

Insertion of Eq. (14) into Eq. (10) yields, after some manipulation, an expression involving the strength and the form factor for the reaction.

$$A_lF_l(r)=-i^lR_0\frac{dV}{dr}\langle J_f\|\alpha_l\|J_i\rangle$$
$$=-i^lR_0\frac{dV}{dr}\left(\frac{\hbar\omega}{2C_l}\right)^{1/2}, \quad (15)$$

for $J_i=0$ and $J_f=l$ and where $F_l(r)$ is the form factor.

Here, V represents the entire optical-model potential as mentioned above. The nuclear deformation parameter β_l, which is frequently used in the literature, is related to the quantities of Eq. (15) by

$$\beta_l^2=(2l+1)\hbar\omega_l/2C_l,$$

and finally, from Eq. (12),

$$\frac{d\sigma}{d\Omega}=\beta_l^2[(VR)_{\text{real}}^2+(VR)_{\text{imag}}^2]\sum_l\sigma_l(\theta), \quad (16)$$

where the $F_l(r)$ is contained in the form of $\sigma_l(\theta)$. A correction to the cross section given by Eq. (16) may be obtained by considering the possibility of Coulomb excitation (C.E.). The calculation procedure is given in Ref. 17, and assumes a multipole charge distribution of the same shape as given by Eq. (13). A correction term to the form factor F_l is then obtained.

An extensive analysis of the inelastic data has been made using a DWBA code developed at Oak Ridge and referred to as JULIE.[36] Various sets of optical-model parameters which satisfactorily describe the elastic data were used as well as several possible form-factor variations for dV/dr in Eq. (15). A summary of the results of this undertaking is given below.

Most analyses of inelastic data for protons, neutrons, and α particles have used the derivative of only the real part of the optical-model potential, and quite reasonable agreement with deformation parameters measured by other means has been obtained.[33–40] More recent work has employed the full complex potential and yielded, in general, a somewhat improved fit to the data, with only slight variations in the value of β_l.[41,42] Identical types of analyses were carried out for the He^3 results with the real form factor (RFF), the complex form factor (CFF), and with the CFF corrected for Coulomb excitations. Figures 11–13 are the results of these calculations, compared with the experimental data.

[36] R. M. Drisko (private communication).
[37] A. Bohr and B. Mottelson, Kgl. Danske Videnskab. Selskab, Mat. Fys. Medd. **27**, No. 16 (1953).
[38] H. Faraggi and J. Saudinos, Argonne National Laboratory Report No. ANL 6848, 1964, p. 137 (unpublished).
[39] P. Darriulat, G. Igo, H. G. Pugh, J. M. Meriwether, and S. Yamabe, University of California Radiation Laboratory Report No. UCRL 11054, 1963 (unpublished); Phys. Rev. **134**, B42 (1964).
[40] H. Crannell, R. Helm, H. Kendall, J. Oeser, and M. Yearian, Phys. Rev. **123**, 923 (1961).
[41] H. W. Broek, J. L. Yntema, B. Buck, and G. R. Satchler, Nucl. Phys. **64**, 259 (1965).
[42] M. P. Fricke and G. R. Satchler, Phys. Rev **139**, B567 (1965).

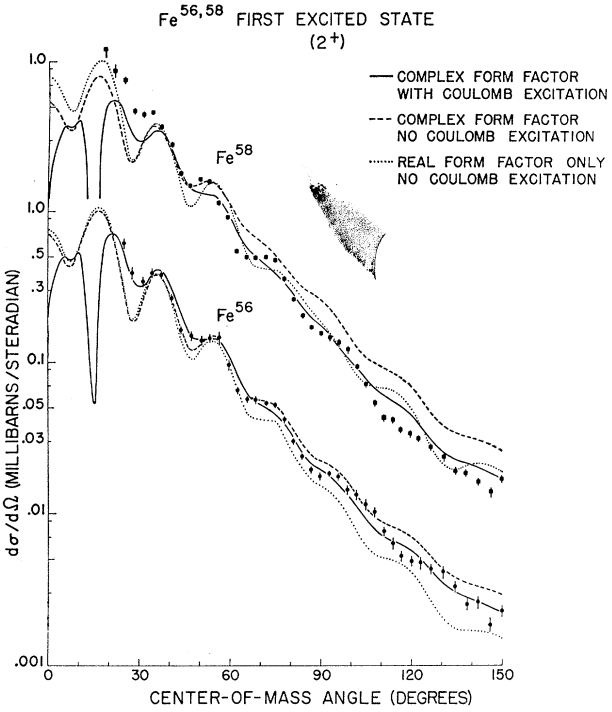

FIG. 11. DWBA fits to $Fe^{56,58}$ 2^+ states.

The values of β_l obtained for the three form factors are listed in Table II along with values obtained previously by other methods. It is quite obvious from this table that for the He^3 interaction, the complex form factor is necessary. Indeed, since the cross section in Eq. (16) is proportional to β_l^2, the table indicates that over 90% of the cross section arises from the imaginary potential rather than from the real potential, in striking contrast to results from nucleon and α-particle scattering experiments. The unusual aspects of these results have been published in a preliminary report.[43] Since the results of the He^3 inelastic scattering were obtained, experiments with deuterons have also produced a somewhat similar result.[44] The β_l's obtained with deuterons differ by a factor of 2 according to whether one uses the CFF or the RFF.

TABLE II. Values of deformation parameters for $Fe^{56,58}$ and Ni^{58} for the 2^+ (β_2) and 3^- (β_3) states.

		RFF[a]	CFF[b]	CFF[b] and CE[c]	CFF[b] and CE[c](ADWBA[d])	Reported values
Fe^{56}	β_2	0.48	0.22	0.19	0.206	0.19 → 0.27
	$\beta_2 R_i$	2.86	1.29	1.12	1.12	0.87 → 1.24
	β_3	0.24	0.11	0.10		0.10 → 0.11
	$\beta_3 R_i$	1.41	0.63	0.60		0.46 → 0.51
Fe^{58}	β_2	0.62	0.22	0.18	0.215	0.17 → 0.25
	$\beta_2 R_i$	3.77	1.31	1.09	1.30	0.79 → 1.16
	β_3	0.23	0.082	0.080		0.08
	$\beta_3 R_i$	1.36	0.50	0.48		0.37
Ni^{58}	β_2	0.58	0.18	0.15	0.175	0.15 → 0.21
	$\beta_2 R_i$	3.63	1.12	0.95	1.08	0.93 → 1.01
	β_3	0.32	0.10	0.10		0.13 → 0.21
	$\beta_3 R_i$	2.04	0.66	0.65		0.86

[a] Real form factor.
[b] Complex form factor.
[c] Coulomb excitation.
[d] Asymmetric distorted-wave Born approximation.

A factor of some importance in extracting accurate values of β_l by the DWBA method is the choice of potentials used in Eq. (11). Since many sets of optical-model potentials can be found which give almost equally good descriptions of the elastic data, it might be expected that the χ's obtained from them in Eq. (11) would give different values of β_l when inserted in Eq. (10). However, this was not found to be the case. At least four different sets of optical-model parameters with V's ranging from 50 to 180 MeV were used in the calculations and the resulting β_l's differed by at most only a few percent. The parameters were chosen, however, to describe the elastic data, for when an arbitrary set is used, the resulting angular distribution has no relation to reality. From these examinations it is seen, therefore, that it is necessary only to describe adequately the incoming and outgoing wave functions. The details of the angular distribution are determined by the interaction mechanism contained in Eq. (15).

2. *Double Stripping*: (He^3,n)

The DWBA method has been very successful in describing the stripping process for single nucleons,[37] and it is natural to attempt its application to the double-stripping process. However, when two nucleons are removed from the incident particle, the complexity of the problem is greatly increased. The interaction can no longer be considered as happening at a point, with the captured particles as a single lump, since they may

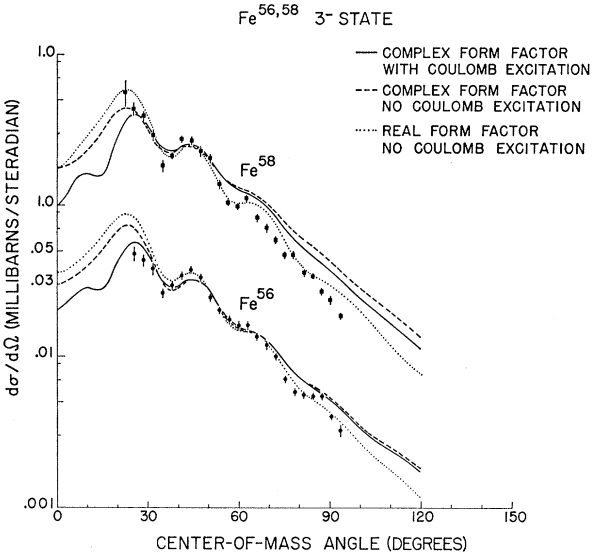

FIG. 12. DWBA fits to $Fe^{56,58}$ 3^- states.

[43] E. R. Flynn and R. H. Bassel, Phys. Rev. Letters **15**, 168 (1965).

[44] J. R. Dickens, F. G. Perey, and G. R. Satchler, Nucl. Phys. **73**, 529 (1965).

very well go into separate orbits in the residual nucleus. In addition, if the wave function describing the final state contains configuration mixing, then a coherent sum must be taken over the various single-particle contributions to this state with a possible large enhancement (or reduction) of the cross section over that expected from single-nucleon stripping. These factors introduce a much greater uncertainty in the resulting calculations. Another unfortunate feature is the mathematical necessity to use a harmonic oscillator well for the captured particles, for it is known that a much better description of the experimental evidence is obtained if a Saxon potential is used to describe the nucleus. The use of the harmonic oscillator is necessitated by the computational requirement to treat separately the relative motion and the center-of-mass motion of the captured particles. This separation can be done only for a finite series of terms in a harmonic oscillator well.[45]

Within the limitations described above, Henley and Yu[14] have carried out an extensive investigation of the present problem, and their results will be used directly.

Referring to Eq. (12), the forms developed by these authors may be obtained if the following expressions are used:

$$A_J = \text{const} \sum_{j_1 j_2} B(j_1 j_2 J, J_i J_f) T^{\dagger}(j_1 j_2 J, J0J) \times H(n0NJ, n_1 l_1 n_2 l_2, J), \quad (17)$$

and

$$F_l(\mathbf{r}) = G d_{NJ}{}^{n*}/(2J+1), \quad (18)$$

where B is the spectroscopic factor which depends upon the initial- and final-state quantum numbers and thus will produce the enhancement factors mentioned above. In Eq. (17), $T^{\dagger}$ is the transformation parameter from L-S to j-j coupling, and H is usually referred to as a Talmi coefficient. It occurs in the transformation to center-of-mass and relative coordinates. In Eq. (18), G depends upon the assumed form of the He^3 wave function and the parameter of the stripping interaction potential which is assumed to be Gaussian. Finally, $d_{NJ}{}^n$ is the wave function of the center of mass of the captured pair of protons.

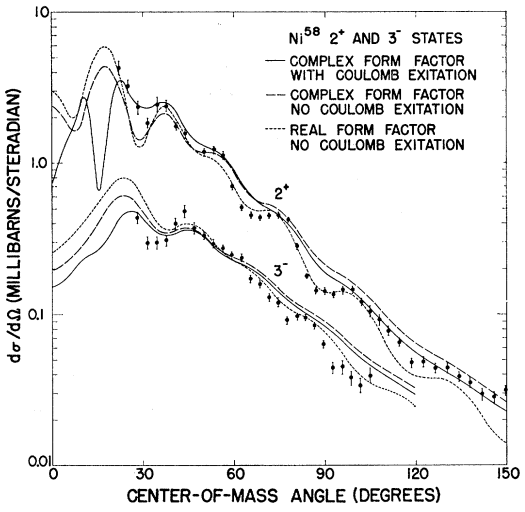

FIG. 13. DWBA fits to Ni^{58} 2^+ and 3^- states.

[45] A. de-Shalit and I. Talmi, *Nuclear Shell Theory* (Academic Press Inc., New York, 1963).

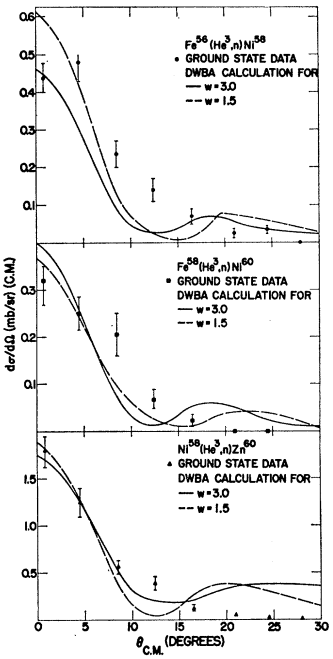

FIG. 14. DWBA fits to ground-state transitions for (He^3,n) reaction on $Fe^{56,58}$ and Ni^{58}.

Again, a code (kindly provided by E. Henley) performs the calculation indicated by Eq. (10) and the final cross section is obtained by means of Eq. (12). A variety of possible A_J's has been tabulated in Ref. 14; these correspond to several possible configurations of the final nucleus varying from simple shell-model to pairing-model considerations. The best fits to the data are shown in Fig. 14, and the fits for the C^{12} and O^{16} targets discussed in the Appendix are shown in Fig. 20.

C. Emission of Low-Energy Neutrons

The theory which best describes the emission of low-energy neutrons from a highly excited complex nucleus is based on the assumptions originally made by N. Bohr, that the decay and formation of a compound nucleus are independent processes and that inside a compound nucleus the interaction among the nucleons is very strong. The cross section for a reaction proceeding by way of a compound nucleus may therefore be written:

$$\sigma(I,O) = \sigma_c(I) G_c(O), \quad (19)$$

where $\sigma_c(I)$ is the cross section for formation of the compound nucleus by an incident particle I and $G_c(O)$ is the probability that this nucleus will then decay into a particular channel designated by O.

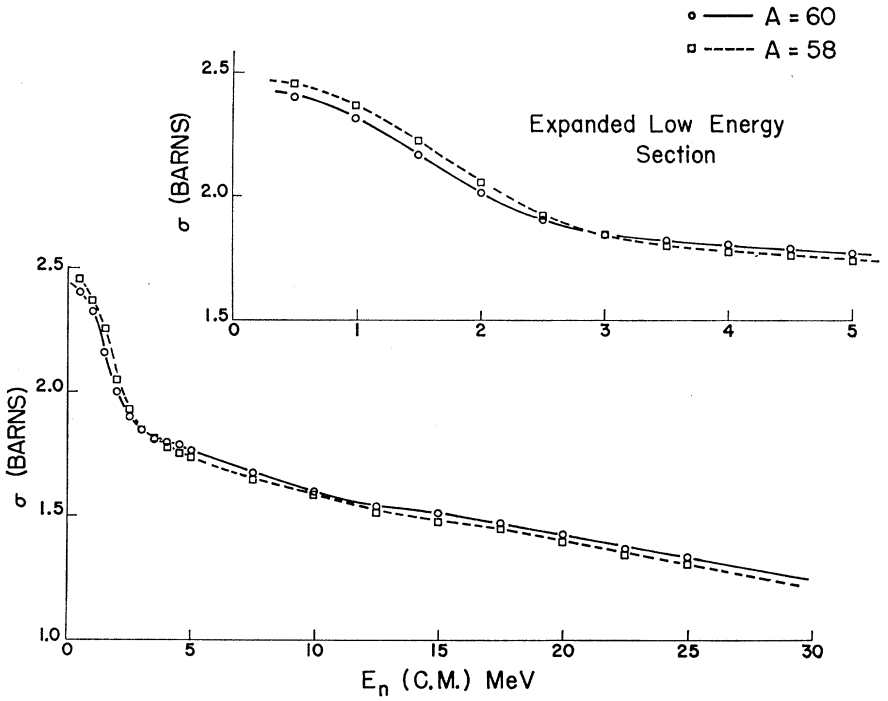

FIG. 15. Predicted compound-nucleus formation cross section.

Starting with this assumption and invoking an additional assumption of random phases, Weisskopf[46] developed the statistical model of the compound nucleus. According to this model, the energy distribution for the emitted neutrons is given by

$$N(E)dE = \text{const} E\sigma_c(O,E)\rho(U)dE, \quad (20)$$

where $\sigma_c(O,E)$ represents the inverse cross section for formation of a compound nucleus by the particle of energy E; $\rho(U)$ is the level density of the residual nucleus at excitation energy U.

Various forms of $\rho(U)$ are found in the literature, depending upon the nuclear model chosen. The most frequently used forms are based upon the Fermi-gas model in which the nucleus is considered as an assemblage of neutrons and protons in a free Fermi gas. An approach based on this model yields the form[47]

$$\rho(U) = U^{-n} e^{2\sqrt{(aU)}}, \quad (21)$$

which, for $n=2$, corresponds to the Fermi-gas model. The nuclear temperature is then defined by

$$\frac{1}{T} = \frac{d}{dU} \ln\rho(U), \quad (22)$$

and, from Eq. (21)

$$\frac{1}{T} = \left(\frac{a}{U}\right)^{1/2} - \frac{n}{U}. \quad (23)$$

Most older work (e.g., Ref. 46) makes use of the approximate relation

$$U = aT^2, \quad (24)$$

which gives an adequate description of much of the experimental data previously obtained. This choice corresponds to $n=0$ in Eq. (21) and yields the elementary Weisskopf evaporation spectrum

$$N(E)dE = \text{const} E\sigma_c(E) \exp(-E/T)dE. \quad (25)$$

It should be noted that Eq. (24) is a reasonable approximation for high-excitation energy, which would make the second term in Eq. (23) small and also would permit the exponential to dominate Eq. (28) Equation (25), however, will not be applicable over a large range of excitation energies.

In most previous analyses of neutron-evaporation spectra, the form of $\sigma_c(E)$ has either been assumed constant or made energy-dependent in accordance with Ref. 46, which is based on a simplified nuclear model. A pref-

TABLE III. Values of the temperature T and level-density parameter a for $Ni^{58,60}$ and Zn^{60} as obtained through the (He^3,n) reaction.

Residual nucleus	Ni^{58}	Ni^{60}	Zn^{60}
Temperature	1.58 MeV	1.68 MeV	1.37 MeV
Level-density parameter a	9.6 MeV^{-1}	9.3 MeV^{-1}	10.0 MeV^{-1}
a corrected for pairing	8.5 MeV^{-1}	8.2 MeV^{-1}	8.4 MeV^{-1}
Average excitation energy	23.9 MeV	26.5 MeV	~18.7 MeV
Excitation of compound nucleus	31.1 MeV	37.6 MeV	~30.4 MeV
Previous values of a when available	Co^{58} by (He^3,p) gives 8.7[a]	Co^{60} by (n,p) gives 8.0±1.5[b]	

[a] Reference 55. [b] Reference 56.

[46] J. M. Blatt and V. F. Weisskopf, *Theoretical Nuclear Physics* (John Wiley & Sons, Inc., New York, 1952).
[47] D. Bodansky, Ann. Rev. Nucl. Sci. 12, 79 (1962).

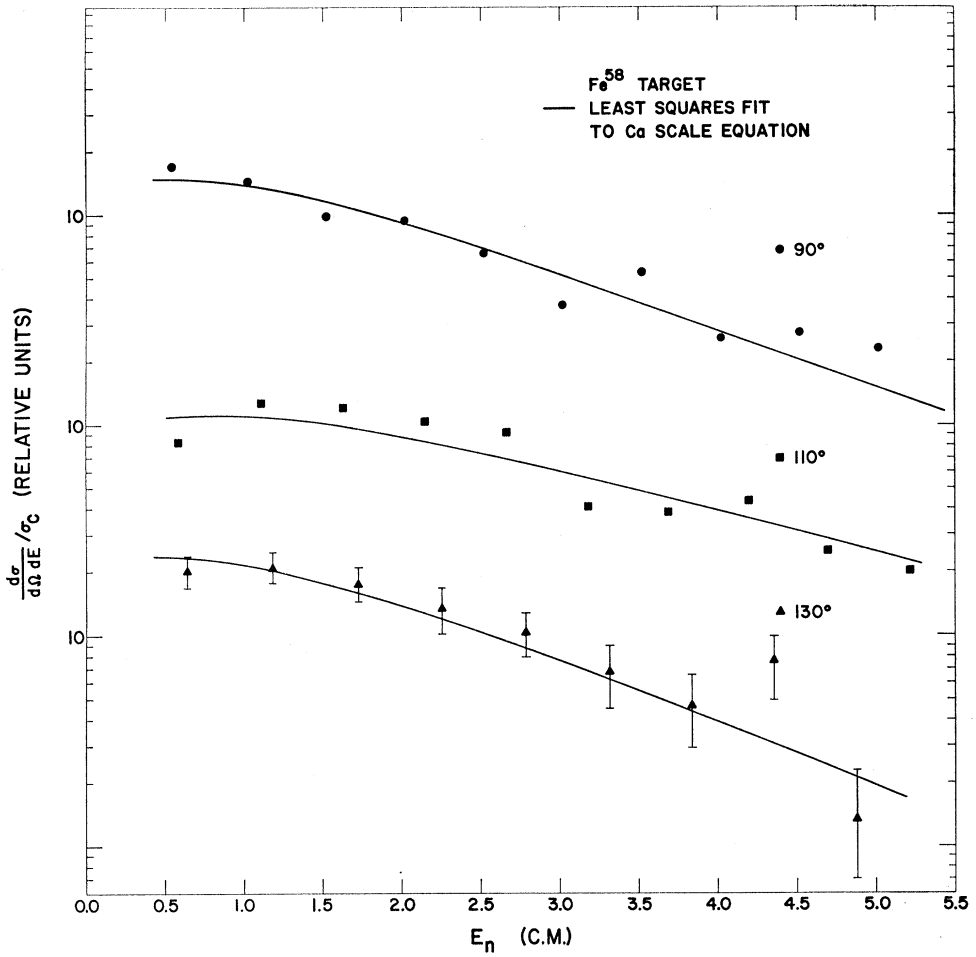

FIG. 16. Typical least-squares fits to evaporation spectra.

erable procedure is to obtain neutron total reaction cross sections as a function of energy. This can be done by using the optical model. The potential adopted here was that of Rosen,[27] who was able to reproduce accurately neutron elastic-scattering data by means of a potential with a single set of average parameters. The potential form used is

$$V(r)=-(49.3-0.33E)[1+\exp(r-1.25A^{1/3})/0.65]^{-1}$$
$$-5.75\frac{d}{dr}\left(2.80[1+\exp(r-1.25A^{1/3})/0.70]^{-1}\right)$$
$$-\left(\frac{\hbar}{m_\pi c}\right)^2\frac{5.5}{r}\frac{d}{dr}$$
$$\times[1+\exp(r-1.25A^{1/3})/0.65]^{-1}\mathbf{l}\cdot\boldsymbol{\sigma}. \quad (26)$$

In Eq. (26), A is the target mass, m_π is the pion mass, and $\mathbf{l}\cdot\boldsymbol{\sigma}$ is the usual spin-orbit term. The energy dependence of $\sigma_c(E)$ thus obtained is shown in Fig. 15.

A correction is necessary to account for pairing forces in nuclei. It has been shown by Newton[48] that this effect may be approximated by decreasing the value of the excitation energy by an amount equal to the pairing energy in the ground-state binding energy. Thus, $U'\sim U-\Delta$, where Δ is the pairing energy. Since only even-even nuclei are considered here, the Δ's may be expressed in the form given by Bodansky[47]:

$$\Delta=3.36(1-A/400). \quad (27)$$

For most of the data considered in this section, there is sufficient excitation energy to allow up to three neutrons to be boiled off, whereas Eq. (25) is adequate only for single-neutron evaporation. Cascades of evaporating particles have been considered by Le-Couteur[49] and he finds that in place of Eq. (25), and under assumption that $U=aT^n$, one should write

$$N(E)dE=\text{const}E^K\sigma_c(E)\exp(-E/t^*), \quad (28)$$

where the values of K and t^* depend upon the value of n in the relation between U and t. Assuming that Eq. (24) is applicable, then $n=2$, $K=5/11$, and $t^*=(11/12)T$; here T is the temperature of the residual nucleus following emission of the first neutron.

[48] T. D. Newton, Can. J. Phys. 34, 804 (1956).

[49] K. J. LeCouteur, Proc. Phys. Soc. (London) **A65**, 718 (1952).

To determine the values of T and a, the following procedure was used. A least-squares fitting program was employed to obtain the best fit of Eq. (28) to the experimental data by varying the constant and t^* until a minimum χ^2 was obtained for the experimental data. This was done for all of the back angles which had been analyzed. The values of the constant and of t^* thus obtained in each case were averaged over the angles to obtain the final t^* and, thus, T. The results for the three elements are shown in Table III. Typical fits to the data, using Eq. (28), are shown in Fig. 16.

The value of the level-density parameter a, given in Eq. (24), now may be found by using the deduced values of T to obtain the average value of the excitation energy U. This average value is found by integrating over the measured spectrum. The result of this procedure is

$$U=U_0-Q-2T, \tag{29}$$

where U_0 is the excitation energy of the compound nucleus and Q is the separation energy for a neutron from the nucleus.

The values of a thus obtained are also given in Table III along with the appropriate average excitation energy. If, in addition, a correction for pairing forces is made as indicated by Eq. (27), the values of a are altered somewhat because of the decreased value of U. These values are also shown in an appropriate column of Table III.

V. DISCUSSION OF RESULTS

In the previous sections were given brief descriptions of the methods used in the theoretical analysis of the experimental data, and the results of these analyses were compared with the observations. The present section will be confined to a discussion of these comparisons.

A. Elastic Scattering

As can be seen from Fig. 9, the optical model provides a satisfactory description of the experimental data. This success is a further demonstration of the wide applicability of the optical-model approach. The application of this formalism to He^3-induced interactions has been discussed previously,[10] and several recent surveys have indicated good agreement with extant data.[8,50] The necessity for five free parameters in this model in order to obtain satisfactory agreement with experiments lessens somewhat the value of this approach. However, as the amount of reliable experimental data increases, systematic surveys may be expected to establish definite trends among the parameters, as in the case of protons (even though the ambiguities among groups of parameters may remain, as is the case for α particles).[16]

[50] R. H. Siemssen, T. H. Braid, D. Dehnhard, and B. Zeidman, Phys. Letters **18**, 155 (1965).

Another possible approach to the description of elastic-scattering interactions lies in the strong-absorption model [Sec. IV (A2)]. The results of this model are shown in Fig. 10, which demonstrates that this method also reproduces the data with reasonable accuracy although not over as wide an angular interval as does the optical model. Only four parameters were used for the strong-absorption calculations, although one must extend this to five or more if nuclear transparencies are included. Inclusion of such additional parameters certainly would lead to an improved fit and perhaps to additional information concerning the nuclear surface. The present four-parameter model suffices to reproduce the main features of the available data.

All of the parameters obtained from the two methods have been listed in Table I. The two sets disagree noticeably in the values of radius and diffuseness, but this is to be expected for strongly absorbed particles such as He^3 ions. The optical-model potential, which is given by Eq. (1), attempts to describe the entire structure of the nucleus including both the interior and exterior wave functions. On the other hand, the strong-absorption model simply relates to the absorption properties of the nucleus, treating it as a black disk with a diffuse edge. It takes account of the effects of the surface upon the phase shifts of the incident beam of particles. Thus, the two methods may describe different regions of the surface. If the absorption is very strong, the absorption radius (inside of which 75% of the particles are absorbed) may well be considerably larger, and the region of absorption considerably sharper, than the

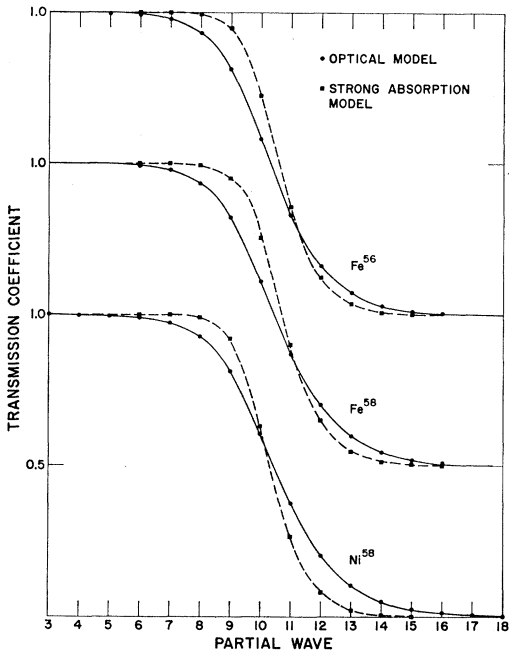

FIG. 17. Transmission coefficients from optical-model and strong-absorption calculations.

corresponding radius and diffuseness given by the optical model. In either case, it must be emphasized that these quantities differ by definition for the two models.

Alster and Conzett[51] have made use of a somewhat different representation of the scattering function, but again the choice is based upon a strong-absorption model. They have compared transmission coefficients for each partial wave of their model with those of the optical model, in the case of α-particle and heavy-ion scattering. From this comparison, they obtained equivalent results for the two models. A similar comparison can be made if the three-parameter model with no spin-orbit term is used since the optical model, as here employed, ignores the $\mathbf{l}\cdot\boldsymbol{\sigma}$ term. This comparison is shown in Fig. 17.

An examination of Fig. 17 indicates that the mean partial wave entering into the interaction is approximately identical for the two models. This is in agreement with the results of Ref. 51. However, the strong-absorption model employed here is considerably more localized in angular-momentum space than is the optical model and in this respect differs from the conclusions of Alster and Conzett. There are several possible explanations for this discrepancy. First of all, the strong-absorption model, which is used here, contains no terms for the transmission of lower partial waves. Another possible explanation lies in the phase shifts, which are generated by the optical model, since there is considerable doubt as to the proper choice of potential to use in this model.

The total reaction cross section in terms of the transmission coefficients is given by

$$\sigma_R=\frac{\pi}{k^2}\sum_{l=0}^{\infty}(2l+1)(1-|T_l|^2), \tag{30}$$

where k is the He^3 momentum and T_l is the transmission coefficient for the lth partial wave. This equation permits a further comparison between the optical model and the strong-absorption model. The results of these two methods are given in Table I and they appear to be in approximate agreement. The poorer fits provided by the strong-absorption model are reflected in the wider variations of these cross sections as compared with the much more consistent results obtained with the optical model.

On one important point there seems to be complete agreement. Both models discussed above suggest that the dominant feature of the elastic-scattering process for He^3 ions is the importance of the absorptive mechanism. In particular, the success of the strong-absorption model in describing the experimental data is a clear indication of this. The results obtained with this model indicate that the interaction occurs within a quite localized region of the nuclear surface and little penetration into the nuclear interior is permitted. The results obtained here and elsewhere with the optical-model approach further substantiate this suggestion. In the case of the optical model, all of the results reported in the literature point to a large value for the absorptive potential W and also a large radius. This has not been the case with the parameters used to describe the real well. The set of parameters used here, which is suggested in Ref. 8, indicates that the scattering radius is characteristic of free nucleons whereas the absorptive radius includes the He^3 contribution. The choice of such a set of parameters thus seems realistic in view of the loosely bound nature of this nucleus and the small probability that such a system would be re-emitted by the target nucleus once it has penetrated to the interior.

B. Inelastic Scattering

The data on the inelastic scattering of He^3 ions have been analyzed here by the DWBA method. The results of this analysis are shown in Figs. 11–13, and in Table II. As has been stated earlier, the interaction mechanism for He^3 ions appears to proceed mainly through the imaginary potential rather than the real, this being perhaps a consequence of the loosely bound nature of this projectile. It is, of course, quite proper to include this absorptive term in the derivative of Eq. (15). Its omission in previous work on proton and α scattering has been mainly for computational convenience.[17] The interaction through the real part of the form factor may be compared to the classical example of a water droplet which is left vibrating after an inelastic collision. The imaginary part of the form factor, however, implies a more subtle mechanism. Thus, when the complete complex potential is used, the nucleus must be thought of as consisting of its composite protons and neutrons, rearranged via their individual interactions with the impinging He^3 nucleus, and leaving the nucleus in an excited state. The probability of formation of any particular excited state is then dependent upon the coupling between the configuration of ground-state nucleons and interacting He^3 ions, and the final excited state. Indeed it is surprising that the model used here works as well as it does since it incorporates only the gross properties of the nucleus and not the individual nucleon contributions. A more sophisticated theory, and one which has a better physical basis, is the random-phase approximation. Recently an attempt has been made to describe inelastic α-particle scattering by this means.[52] However, as has been shown, the theory used here does produce a good description of the data as well as deformation parameter values which agree remarkably well with values obtained by completely different techniques (see Table II).

There is another interesting feature of Figs. 11–13. If one examines the comparative fits to the data for the

[51] J. Alster and H. E. Conzett, Phys. Rev. **139**, B50 (1965).

[52] V. A. Madsen and W. Tobocman, Phys. Rev. **139**, B864 (1965).

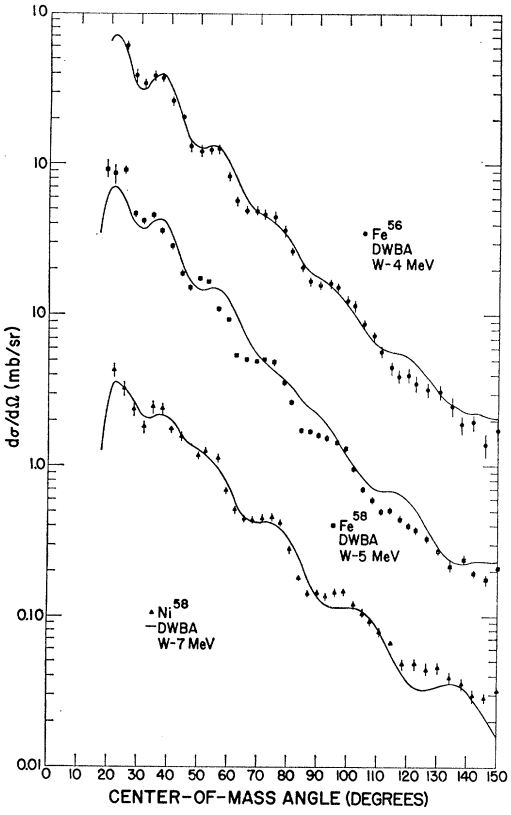

FIG. 18. Asymmetric DWBA fits to 2^+ states of $Fe^{56,58}$ and Ni^{58}.

RFF case and CFF case, the RFF fit is noticeably as good or better than the CFF. This implies that the nuclear potential has the same shape for both real and imaginary parts at the interaction radius. This was indicated previously by the approximate equality of real and imaginary diffuseness parameters in the elastic-scattering analysis. Actually, the poorness of fit for the CFF, even though giving the correct values of β_l, is somewhat misleading. Since the effect of W is so large here, it might be expected that the same value of W should not be used on both sides of the overlap integral of the DWBA calculation. The use of a symmetric form of this overlap integral is common in such computations and is based on the assumption that there is very little difference between the optical-model potential for the ground and excited states, and this indeed has been found to be true for inelastic proton scattering.[53] Because of the strong effect of W in the present investigations, it was decided to determine whether an improvement in the over-all fit could be found by changing its value in the exit channel. W was therefore varied in 1-MeV steps for the final state of the DWBA calculation, and the resulting distributions compared to the data. Substantially improved fits were obtained in this way as can be seen in Fig. 18. The new values of the deformation parameter obtained using this asymmetric formulation (ADWBA) are given in the appropriate column of Table II. In all cases, the value of W was reduced to obtain the best fit, indicating that the 2^+ state is coupled less strongly to the other excited states than is the ground state. This probably arises because the 2^+ state is coupled to the ground state with the same strength in both the entrance and the exit channels. Thus, only the difference of coupling to all other excited states affects the value of W. Such an effect, to the authors' knowledge, has not been previously observed. A similar examination of the 3^- states found the coupling sufficiently weak that it was impossible to see an improved fit by reducing or increasing W.

[53] F. Perey and G. R. Satchler, Phys. Letters **5**, 212 (1963).

C. Double-Stripping Interaction

The results obtained from the application of the double-stripping theory of Ref. 14 are quite poor, making discussions of the reaction mechanism inconclusive. The experiment proved quite difficult because of the low cross sections encountered and the need to distinguish the ground state from low-lying excited states of the daughter nucleus.

An additional uncertainty, which occurs because of the poor agreement between theory and experiment, is in the proper choice of the oscillator parameter ω which is chosen to give the best representation of the data. In Ref. 14, it was found that a value of 3 MeV permitted agreement with the data of Manley.[6] In the Appendix, a value of 2 MeV is obtained when comparisons to data from C^{12} and O^{16} targets are made. These data are, however, at a slightly higher energy than those of Manley. For purposes of comparison, calculations at $\omega=3$ MeV were performed and the results are shown in Fig. 14. In addition, a set of calculations at $\omega=1.5$ MeV is also shown. This latter value of ω produced the most consistent description of the data out of a large range of values examined. When compared with the results of Ref. 14, taking account of the most appropriate values of ω and the He^3 energy, the spectroscopic values could be obtained. These however must be considered as crude estimates, because the quality of fit as shown in Fig. 14 did not allow an accurate normalization number to be obtained. For Ni^{58}, the spectroscopic value $B=0.012$ for $\omega=1.5$ and $B=0.2$ for $\omega=3.0$; for Fe^{58}, $B=0.002$ for $\omega=1.5$ and $B=0.0005$ for $\omega=3.0$; and, finally, for Fe^{56}, $B=0.0026$ for $\omega=1.5$ and $B=0.0014$ for $\omega=3.0$.

Although these values must be considered as only approximations, the variance between the Ni^{58} target result and the result obtained by Henley and Yu is substantial enough to rule out their prescription for the wave function of the residual nucleus. For this case, they assumed a pairing model for the Zn^{60} nucleus and obtained a value for B of 0.22. The present result of either 0.012 or 0.02 is closer to the value obtained for a pure shell-model configuration consisting of two $1f^{5/2}$

particles. However, the actual configuration most likely consists of a mixture of states dominated by the $2p^{3/2}$ and the $1f^{5/2}$ states but with destructive interference occurring and producing the low cross sections observed. The present data do not suffice to allow the determination of the relative amounts of configuration mixing present.

The results for the light isotopes C^{12} and O^{16} are in much closer agreement with the theory. These results have been included in the Appendix to indicate that the double-stripping theory does indeed provide a reasonable representation of the experimental data when the cross sections involved are sufficiently high and when adequate wave functions for the nuclei involved are available.

A possible explanation for the discrepancy between the theoretical and experimental angular distributions lies in the optical-model parameters employed in describing the He^3 particle in the entrance channel of the DWBA calculation. The computer code which performed this operation required the use of a potential in which the real and imaginary geometrical parameters were identical. Thus, the form and the parameters for the potential obtained in Sec. IV A1 are not applicable. Fortunately, the neutron potential given in Eq. (33) is of a form which is permitted by the code, and the exit-channel requirements could be satisfied. To obtain the necessary He^3 optical-model parameters for this calculation, a search was performed in which the real and imaginary geometrical parameters were held equal. Thus, four quantities were varied—V, W, R, and a—and a minimum χ^2 with the experimental data was obtained. The parameters are: Ni^{58}, $R=1.56$F, $a=0.66$F; Fe^{58}, $R=1.49$F, $a=0.68$F; Fe^{56}, $R=1.54$F, $a=0.69$F; and $V=30$ MeV, $W=25$ MeV for all three targets. The resulting fit to the data was substantially poorer than with the parameters given in Table I.

A recent investigation has pointed out that the double-stripping reaction is particularly dependent upon the choice of optical-model potentials.[54] In contrast to single-nucleon stripping where the differential cross sections are relatively insensitive to the potential, these authors found a marked dependence on the triton potential when describing (t,p) data. The (He^3,n) case should be completely analogous to the (t,p) reaction. Furthermore, they find that real potentials on the order of 150 MeV are necessary and that a potential of 50 MeV produces a poor fit. In the present case, it was not possible to use such a potential while simultaneously maintaining equal real and imaginary geometries. Thus, it may well be that if the potential of Table I had been used, an improvement in the fit to the experimental data would have been obtained. It is not known how this affects the magnitude of the spectroscopic factor, although it is unlikely that the large discrepancy found here could be completely eliminated by this means.

D. Compound-Nucleus Formation

Evidence for compound-nucleus formation is provided by the low-energy neutrons emitted at large angles. Fitting the data to evaporation spectra gives temperatures and level-density parameters which agree well with previously established values, wherever a comparison is possible. A correction for pairing forces and the use of a cascade formula for multineutron emission are necessary to arrive at a satisfactory representation of the data.

Of particular interest is the approximate agreement of the results for the level spacing of Ni^{58} with those previously reported for Co^{58} in Ref. 55. The latter data were also corrected for pairing energy to obtain the final level-density values. Ni^{58} represents a closed proton-shell configuration, whereas Co^{58} is an odd-odd nucleus with one proton hole. At low excitation energies, the level density is certainly much greater for the Co^{58} nucleus than for Ni^{58}. The present experimental results indicate that the level densities become equal at high excitation. Thus, it can be inferred that the level-density parameter in the region of the closed $F^{7/2}$ shell is dominated by the compound-nucleus mechanism when the excitation energy is sufficiently high. This confirms the results of a previous investigation[49] in which it has been shown that the level-density parameter is essentially independent of excitation energy above the region of nonoverlapping levels for the nuclei under consideration.

The results obtained for Ni^{60} and Zn^{60} also substantiate the above interpretation. The level-density parameters given in Table III are again in close agreement with each other. A further comparison to these two nuclides is given by the Co^{60} result shown in the table,[56] which was obtained by an (n,p) reaction. The agreement here is well within the experimental accuracies, and the results indicate no observable deviations in level densities as one passes through a closed shell, indicating once more that shell effects do not dominate the level structure at high excitation energies.

It should be observed that the (He^3,n) reaction offers a useful tool for the observation of compound nuclear processes in a variety of nuclei previously unexplored. These nuclei will, in general, be proton-rich and a study of their properties in comparison to neutron-rich nuclei obtained, for example, by (t,p) reactions would be of considerable interest.

VI. SUMMARY

The present experiments were undertaken to explore the nature of the He^3 interaction and, in so doing, to arrive at a better understanding of the dominant inter-

[54] R. N. Glover and A. D. W. Jones, Phys. Letters **18**, 165 (1965).

[55] J. Hazan and G. Merkel, Phys. Rev. **139**, B835 (1965).

[56] D. W. Lang, Nucl. Phys. **26**, 434 (1961).

action mechanisms. A secondary objective was to investigate the utility of He^3 ions as a nuclear probe. Several of the experimental endeavors discussed above did indeed yield results which differ markedly from those previously obtained with other projectiles and permit new insight into the general problem of nuclear interactions. Certainly the strong absorption of the He^3 ion seems well established as is also the phenomenon that He^3 scattering processes occur at a rather large radius. The present data offer convincing evidence that the scattering processes are dominated by the imaginary or absorptive potential. The value of the He^3 projectile as a nuclear probe is enhanced because of information obtainable from (He^3,n) reactions, both with respect to studies of compound nuclei and of the configurations of residual nuclei following two-particle stripping.

Because it is strongly absorbed, the He^3 nucleus seems ideally suited for use as a probe of the nuclear surface. The elastic-scattering data, when analyzed by the optical model, yield a large imaginary radius with a deep well which seems to dominate the scattering process. The strong-absorption model yields results in support of the above and indicates a sharply defined interaction near the surface and inside of which the He^3 nucleus is completely dissolved. The effect on the inelastic scattering of this surface absorption is quite evident. Indeed, for this process, the real well depth is almost of negligible importance. All of these results then indicate that the interior of the nucleus is opaque to He^3 particles, and such particles therefore are completely unsuited for the investigation of the nuclear interior.

The detailed examination of the neutrons emitted from the three target nuclei here considered indicates that, at the high excitation energy end of the spectrum, compound-nucleus effects dominate the various energetically possible kinds of interactions. At the low excitation energies, direct interactions are of primary importance as expected, but they proceed with much lower cross sections than had been predicted. In the compound-nucleus studies it was found that the cascade formula used for multiple neutron emission gives a quite reasonable description of the low-energy neutron spectra. Furthermore, level-density parameters were found which are consistent with previous measurements involving the same residual nuclei, and also with measurements leading to the same atomic mass number, but different neutron-proton ratios. This last fact is interpreted as indicating the absence of shell-structure effects at high excitation. The low cross sections obtained for the ground-state transitions indicate the absence of enhancement due to pairing forces between the captured protons. A simple shell model seems adequate to reproduce the observed cross sections.

ACKNOWLEDGMENTS

We wish to express our appreciation to the P-10 microscopy section for their help in the data analysis and also to the Los Alamos cyclotron group for their cooperation in this program. We are indebted to A. G. Blair, R. H. Bassel, E. M. Henley, and H. C. Bryant for many helpful discussions.

APPENDIX

In addition to the neutron energy spectra and angular distributions already shown for $Fe^{56,58}$ and Ni^{58}, several other targets also were used during these experiments. These targets were used to establish the neutron-counter energy scale which is shown in Fig. 1, and in the case of C^{12} and O^{16}, angular distributions were also measured to further establish the validity of the double-stripping code.[14]

Figure 19 shows the energy spectra for three of the calibration targets. The lowest energy points obtained are given in the Ne^{18} spectrum, where the ground state and first excited states are well resolved. O^{14} then yields an intermediate point (close to the Zn^{60} ground-state

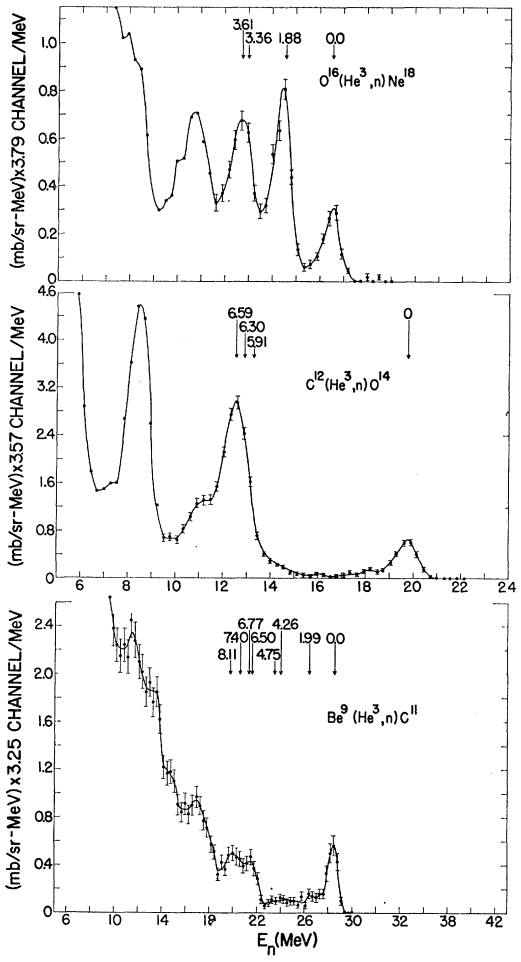

FIG. 19. Energy spectra of (He^3,n) reaction on C^{12}, O^{16}, and Be^9 at 0°. The ordinate is related to the absolute cross section as indicated; this choice is such that the total cross section for a level may be found by summing the indicated experimental points in that level.

energy), and the large group representing the first three excited states is also a convenient check point. To establish a high-energy calibration point for checking the positions of the levels from the Fe targets, Be^9 was chosen, and the resulting ground state of C^{11} is shown in the lowest group of Fig. 19.

Considerable effort has been applied to the level structure and spin assignments of the light nuclei and, because of this, the spectroscopic factors are better known than in the case of the iron and nickel isotopes. To this date, there has been only meager experimental evidence to support the theory of Henley and Yu,[14] and because of this the number of angular distributions measured were extended to include C^{12} and O^{16} as targets. With these data, and the more accurate spectroscopic factors, it is then possible to obtain a reasonable check of the theory which would in turn give more confidence in the $Fe^{56,58}$ and Ni^{58} comparisons. Extensive discussion of these light targets has been given in Ref. 14 and the appropriate spectroscopic factors are listed therein.

Figure 20 contains the results of a DWBA calculation for the ground-state transition for $C^{12}(He^3,n)O^{14}$ and both the ground and first excited states of $O^{16}(He^3,n)$-Ne^{18}. The spectroscopic factors required for the ground-state fits are 0.09 for O^{14} and 0.46 for the ground state of Ne^{18}. The fit to the first excited state is very poor and no spectroscopic factor was calculated; however, the same normalizing constant which was applied to the ground state is also used for this state.

The theoretical curves obtained in this section employed a harmonic oscillator energy of 2 MeV rather than the 3 MeV which was used in Ref. 14. Superior fits to the data were obtained for $\omega=2$ MeV. Extraction of spectroscopic factors have included corrections for the variance in energy and the value of ω between the present data and the cases considered in Ref. 14. The values obtained above should be compared to 0.048 for O^{14} and 0.37 as given in the reference. The agreement here is considered satisfactory in view of the many difficulties involved in obtaining absolute theoretical cross sections.

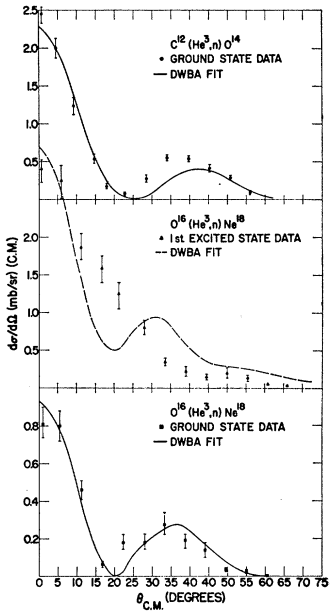

FIG. 20. Angular distribution and DWBA fits to states of O^{14} and Ne^{18}.